Thermal resistance of heated superhydrophobic channels with streamwise thermocapillary stress

Samuel D. Tomlinson*
Department of Mathematics,
University of Manchester,
Manchester, M13 9PL, UK
Email: samuel.tomlinson@manchester.ac.uk

Michael D. Mayer
Department of Mathematics,
Imperial College London,
London, SW7 2AZ, UK
Email: m.mayer@imperial.ac.uk

Toby L. Kirk
Department of Mathematics,
Imperial College London,
London, SW7 2AZ, UK
Email: toby.kirk12@imperial.ac.uk

Marc Hodes
Department of Mechanical Engineering,
Tufts University,
Medford, MA 02155, USA
Email: marc.Hodes@tufts.edu

Demetrios T. Papageorgiou
Department of Mathematics,
Imperial College London,
London, SW7 2AZ, UK
Email: d.papageorgiou@imperial.ac.uk

A pressure-driven channel flow between a longitudinally-ridged superhydrophobic surface (SHS) and solid wall is studied, where a constant heat flux enters the channel from either the SHS or solid wall. First, a model is developed which neglects thermocapillary stresses (TCS) in the transverse direction. The caloric, convective and total thermal resistance are evaluated and their dependence on the shape of the liquid–gas interface (meniscus), gas ridge width, texture period, channel height, streamwise TCS, Péclet number and channel length is established. The caloric resistance is minimised with menisci that protrude into the gas cavity, large slip fractions, small channel heights and small streamwise TCSs. When heating from the SHS, the convective resistance increases, and therefore, a design compromise exists between caloric and convective resistances. However, when heating from the solid wall, the convective resistance remains the same and SHSs that minimise caloric resistance are optimal. We investigate both water and Galinstan for microchannel applications and find that both configurations can have a lower total thermal resistance than a smooth-walled channel. Heating from the solid wall is shown to always have the lowest total thermal resistance. Numerical simulations are used to analyse the effect of transverse TCSs. Our model captures much of the physics in heated superhydrophobic channels, but is computationally inexpensive when compared to the numerical simulations.

*Corresponding author.

NOMENCLATURE

A	dimensionless strength of thermocapillary stress
$\mathcal{A}^*$	cross-section area
a^*	half dimensional groove width
α	thermal diffusivity
$Ca_\perp$	transverse Capillary number
d^*	half dimensional ridge period
δ	gas fraction
γ	surface tension constant
Γ	ratio of Péclet number to dimensionless channel length
h^*	dimensional channel height
h	dimensionless channel height
k	thermal conductivity
L^*	dimensional channel length
L	dimensionless channel length
μ	dynamic viscosity
$\boldsymbol{n}$	normal vector
Nu	Nusselt number
Nu_{B}	plane-flow Nusselt number
$\widehat{Nu}$	normalised Nusselt number
p^*	dimensional liquid pressure
$Pé$	Péclet number
Pr	Prandtl number
Q^*	dimensional flow rate
Q	dimensionless flow rate
Q_{B}	plane-flow flow rate

$\widehat{Q}$ normalised flow rate
q''_{sl} dimensional heat flux per unit area on heated surface
φ protrusion angle
φ_A advancing protrusion angle
ρ density
$Re_{\perp}$ cross-plane Reynolds number
Re Reynolds number
R_{φ} radius of curvature of the meniscus
R^* dimensional total thermal resistance
R dimensionless total thermal resistance
R_{B} plane-flow total thermal resistance
$\widehat{R}$ normalised total thermal resistance
$\mathcal{S}$ shape of meniscus
σ coefficient of surface tension
σ_0 constant in surface tension expression
θ^* dimensional temperature
θ dimensionless temperature
θ^*_{m} mixed-mean temperature
$\bar{\theta}^*_{\mathrm{s,out}}$ average surface temperature at $x^* = L^*$
$\theta^*_{\mathrm{m,in}}$ mixed-mean temperature at $x^* = 0$
θ^*_0 constant in surface tension expression
$\boldsymbol{t}$ tangent vector
$\boldsymbol{u}^*$ dimensional velocity vector
$\boldsymbol{u}^*_{\perp}$ dimensional cross-plane velocity vector
u^* dimensional streamwise velocity
u dimensionless streamwise velocity
v^* dimensional normal velocity
w^* dimensional transverse velocity
x^* dimensional streamwise coordinate
y^* dimensional normal coordinate
y dimensionless normal coordinate
z^* dimensional transverse coordinate
z dimensionless transverse coordinate

1 Introduction

In recent years, it has been established that superhydrophobic surfaces (SHSs) may be employed in a channel flow to reduce drag [1]. The internal liquid is suspended in the Cassie–Baxter state, such that a liquid–gas interface is maintained over some microscopic surface topography with hydrophobic surface chemistry [2]. Evidence of drag reduction in both laminar and turbulent flows can be found in the reviews [1,3,4]. Of interest here is laminar flow in a channel structured with longitudinal ridges (which have been shown to be optimal compared to transverse ridges or pillars [5]). Early works assumed flat liquid–gas interfaces (menisci), but it has been shown in [6, 7] that constant curvature menisci can affect the drag reduction, and their inclusion—as pursued here—is important.

A promising application of SHSs is in the thermal management of microelectronics, where a liquid flow is used to carry heat away from the solid structure in a microchannel cooling configuration [8]. For a channel consisting of a SHS on one side and a smooth wall on the other, there exists two possible configurations: (i) heat entering the liquid from the SHS (with the smooth wall adiabatic) and (ii) heat entering from the smooth surface (with the SHS adiabatic). For (i), the solid–liquid contact area is reduced, thus increasing the flow rate and the ability to carry heat away efficiently (decreased *caloric* resistance). At the same time, the Nusselt number is reduced (increased *convective* resistance) due to the smaller contact area. Consequently, it is the *total thermal resistance* (the sum of convective and caloric resistances) that needs to be minimised in applications, and the present study addresses this optimisation problem for the first time. Our goal is to find channel geometries (and liquids) that allow for better cooling than smooth channel walls. We also investigate (ii) for the first time, as an alternative to (i), for minimising the total thermal resistance in microchannel applications.

Complications arise due to the physics associated with SHSs. Thermocapillary stresses (TCSs) are generated due to temperature variations in the streamwise and transverse directions, which can adversely affect the drag reduction as discussed previously [9]. In the current work, meniscus curvature and streamwise TCSs will be taken into account in a consistent way. To reduce the complexity of the problem and allow a wide parametric study, we will ignore the weak variations in meniscus curvature in the streamwise direction due to the pressure gradient that drives the flow—see [10] for an asymptotic analysis of the isothermal problem. The gas phase beneath the meniscus and its interaction with the internal liquid will also be neglected [11,12], as well as evaporation and condensation along the meniscus and the transverse TCS in (i) where we heat from the SHS. In (ii), where heating occurs from the solid wall, there is only minimal transverse variation in temperature at the menisci. Using numerical simulations, we will show that transverse TCSs are weak in the applications considered here [13]. Our central methodology, which neglects these stresses, offers a computationally cheaper alternative to these numerical simulations, whilst capturing a significant amount of the dominant physics.

Many previous studies have assessed the applicability of SHSs in heat transfer. Upon assuming that the flow is hydrodynamically and thermally fully developed, [14] found expressions for the Nusselt number in a pressure-driven flow with slip boundary conditions. Evidence from [14, 15] suggests that the majority of heating at the SHS occurs through the solid ridge, with the gas cavity acting as a layer of insulation. Motivated by these studies, in case (i) we assume that heating via the SHS occurs exclusively through the ridges and not the gas cavity. A numerical study under fully developed thermal conditions was carried out by [16] for the transversely ridged problem, where they found that the Nusselt number does not exceed that of a smooth channel. In [17], a solution is obtained via a decomposition of the temperature and pressure fields into a linear and periodic component, which relies on the flow being fully developed [18]. In [19], a slip profile was used for the velocity field; however, the temperature field was solved directly to find the Nusselt number. This assumption was removed by [20], who showed that the slip profile breaks down when the channel height is not large. Assuming an isoflux condition, the fully developed assumption allows us to decompose the temperature field into a streamwise linear component and transverse component. The temperature field is then resolved numerically without approximating the velocity field with a slip profile.

Galinstan has been considered as an alternative liquid for the microchannel cooling of electronic components due to its preferred thermophysical properties [13]. Most importantly, its thermal conductivity is thirty times greater than that of water [21]. To quantify the relative balance between the advantages and disadvantages of SHSs, and compare Galinstan and water as working liquids, [22] combined results for both the caloric and convective resistance. For Galinstan, they found that the benefits to the caloric resistance outweighed the detriments to the convective resistance, such that SHSs reduced the total thermal resistance when compared to a smooth-walled channel. In addition, the surface tension and advancing contact angle of liquid metals are higher than that of water. For Galinstan, this allows for twenty times the pressure difference to be imposed whilst maintaining a liquid–gas interface in the Cassie-Baxter state, and allows for larger protrusion angles at the meniscus [23]. In this study, we compare both water and Galinstan by calculating the total thermal resistance, whilst using parameters that are characteristic of the thermal management of microelectronics.

The introduction of Marangoni stresses into a SHS model was first considered by [24] for liquid droplets. Then, [25] analysed their effect on the slip length in the case when the temperature gradient alone drives the flow (unlike the pressure-driven flows considered here). For moderate temperature gradients along the liquid–gas interface, the stresses drive the flow at considerable speed. If we return to consider a pressure-driven flow in a longitudinally ridged SHS channel, the linear increase in temperature along its length generates a streamwise TCS that reduces the flow rate. [9] took into account the components of TCS parallel and perpendicular to the ridges in a SHS channel, showing how they could directly impact the flow rate. Only one wall was structured and the menisci were assumed flat which allowed for exact solutions to be found for the streamwise velocity field. Meniscus curvature was incorporated into the problem by [13]. Assuming a small transverse Reynolds number, defined therein, the streamwise and transverse flow fields decouple. The streamwise TCS is constant in this case and depends on the streamwise velocity field. This makes the problem nonlinear and results in the existence of solutions for streamwise TCSs below a maximum value, which is identified. These asymptotic solutions are shown to compare favourably with numerical simulations. We extend the model in [13] to evaluate the Nusselt number and total thermal resistance for any channel height, slip fraction and protrusion angle, whilst also accounting for streamwise TCS.

This paper investigates the combined effects of the channel geometry, streamwise TCS and meniscus curvature on the total thermal resistance of a heated channel that is bounded between a longitudinally ridged SHS and solid wall. The heating occurs from either the SHS or solid wall. An efficient numerical technique is deployed to solve our model, which includes a domain decomposition and singularity removal at the triple-contact points. This allows us to optimise channel geometries and liquid properties that can be beneficial for applications in the thermal management of microelectronics. Our model is inexpensive when compared to numerical simulations of the more general problem also accounting for transverse TCSs. Finally, we use these numerical simulations to highlight some of the additional physical effects in the problem and give a boundary of validity to our model.

The paper is arranged as follows. In Sec. 2, we formulate the problem for heated SHS channels with longitudinal ridges. In Sec. 3, we define the quantities used to characterise the total thermal resistance. In Sec. 4, we discuss the numerical method and validate our code. In Sec. 5, we present results on the caloric, convective and total thermal resistance. We then make predictions for thermal management in microchannel applications and compare to numerical simulations capturing transverse TCSs. In Sec. 6, we summarise our study.

2 Formulation

2.1 Governing equations

We consider a laminar diabatic flow in a parallel-plate channel, where the bottom wall is structured with longitudinal ridges (aligned parallel to the flow direction) and the top wall is a flat no-slip surface, see Fig. 1. It is assumed that surface tension maintains a Cassie-Baxter state, where the liquid is pinned at the ridge tips above a trapped gas phase [2]. The pressure difference at the liquid–gas interface (meniscus) means that it forms a circular arc ($\mathcal{S}$), which may point into or out from the gas cavity at a given angle φ (note that $\varphi > 0$ corresponds to protrusion into the cavity) [26]. There are a large number of ridges, which means that transverse periodicity holds over most of the domain and sidewall effects can be neglected [12]. Due to periodicity, and also symmetry about the centreline of each period window, we only need to consider one half of one period, which has width d^* and height h^*, where the (half) width of the gas cavity is a^*. The liquid is driven by a pressure gradient $\partial p^*/\partial x^*$ that is constant in the streamwise (x^*) direction over a length of channel L^*. A constant heat flux at either: (i) the top of the ridges or (ii) the channel lid, supplies thermal energy into the liquid and the menisci are assumed to be adiabatic. The temperature on the meniscus therefore increases in the streamwise direction and decreases in the transverse (z^*) direction (from the ridge corner, $z^* = a^*$, to the centre of the meniscus, $z^* = 0$). The opposite occurs for the surface tension, inducing streamwise and transverse TCSs at the meniscus.

Assuming that the flow is hydrodynamically and thermally fully-developed in the streamwise direction, x^*, and steady in time, then the velocity field is independent of x^*, i.e. $\boldsymbol{u}^* = (u^*(y^*, z^*), v^*(y^*, z^*), w^*(y^*, z^*))$, and the temperature field is $\theta^*(x^*, y^*, z^*)$. The dimensional mass conservation, momentum and thermal energy equations in

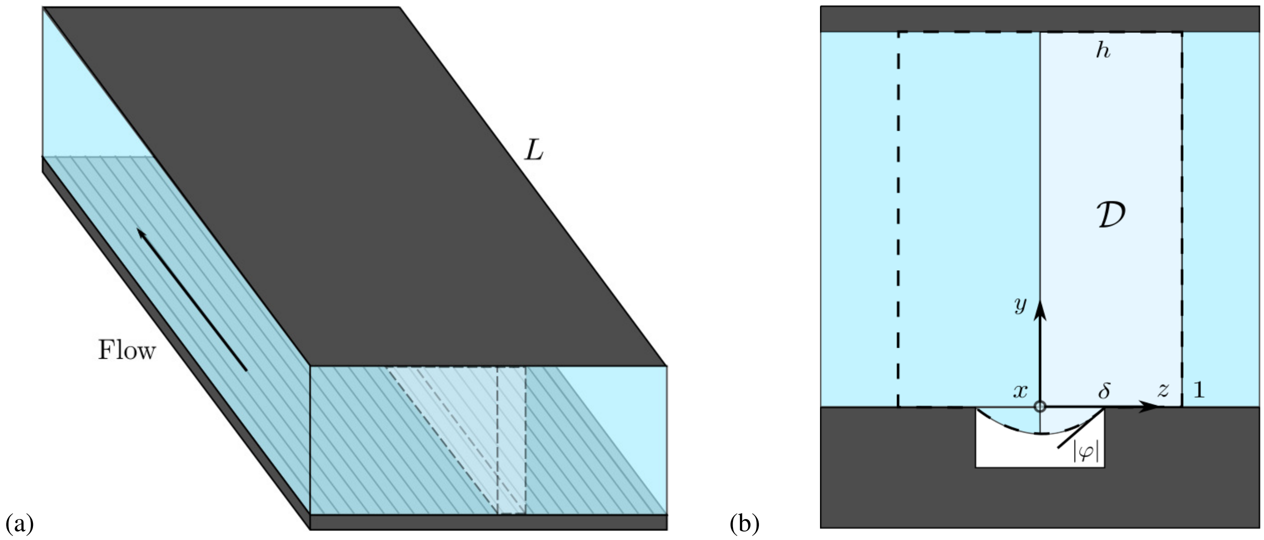

Fig. 1. Schematics of the problem: (a) depicts the heated channel flow bounded between a SHS and solid wall, and (b) the periodic domain, $\mathcal{D}$, corresponding to half of one period; the boundary is indicated by the solid black line. In the above figure: h is the channel height, δ is the slip fraction, φ is the protrusion angle (a positive sign indicates deflection into the gas cavity) and the dashed line contains one period. The dark grey areas indicate the solid, the blue the liquid, and the white the gas region.

the (liquid) domain are given by

$$\boldsymbol{\nabla}_\perp^* \cdot \boldsymbol{u}^* = 0, \tag{1a}$$

$$\rho\, \boldsymbol{u}_\perp^* \cdot \boldsymbol{\nabla}_\perp^* \boldsymbol{u}^* = -\boldsymbol{\nabla}^* p^* + \mu {\nabla_\perp^*}^2 \boldsymbol{u}^*, \tag{1b}$$

$$\boldsymbol{u}^* \cdot \boldsymbol{\nabla}^* \theta^* = \alpha {\nabla_\perp^*}^2 \theta^*, \tag{1c}$$

where $\boldsymbol{u}_\perp^* = (v^*, w^*)$, $\boldsymbol{\nabla}_\perp^* = (\partial/\partial y^*, \partial/\partial z^*)$, ${\nabla_\perp^*}^2 = \partial^2/\partial {y^*}^2 + \partial^2/\partial {z^*}^2$, ρ is the density, μ is the dynamic viscosity and α is the thermal diffusivity.

At the top wall, $y^* = h^*$ for $z^* \in [0,\, d^*]$, and on the tops of the solid ridge, $y^* = 0$ and $z^* \in [a^*,\, d^*]$, we have no-slip and impermeability,

$$\boldsymbol{u^*} = \boldsymbol{0}. \tag{2}$$

On the meniscus portion of the SHS, i.e. $y^* \in \mathcal{S}$ and $z^* \in [0,\, a^*]$, the assumptions and boundary conditions are as follows. We assume that (i) the effects arising from the non-condensable gas or vapour which may be present in the grooves are negligible; (ii) variations in streamwise meniscus curvature are small as the channel length is commonly much greater than its height; and (iii) the surface tension can be approximated as a linear function of temperature, $\sigma = \sigma_0 - \gamma(\theta^* - \theta_0^*)$, where σ_0, γ and θ_0^* are constants. The reader is referred to [13] where (i)–(iii) are discussed in more detail for both water and Galinstan. The tangential stress balances in the streamwise and transverse directions, impermeability, and the adiabatic condition are given by, respectively,

$$\mu \boldsymbol{n} \cdot \boldsymbol{\nabla}^* u^* = \gamma \frac{\partial \theta^*}{\partial x^*}, \tag{3a}$$

$$\mu \boldsymbol{t} \cdot \left(\boldsymbol{\nabla^*} \boldsymbol{u}_\perp^* + (\boldsymbol{\nabla^*} \boldsymbol{u}_\perp^*)^T \right) \cdot \boldsymbol{n} = \gamma \boldsymbol{t} \cdot \boldsymbol{\nabla^*} \theta^*, \tag{3b}$$

$$\boldsymbol{n} \cdot \boldsymbol{u^*} = 0, \tag{3c}$$

$$\boldsymbol{n} \cdot \boldsymbol{\nabla}^* \theta^* = 0, \tag{3d}$$

where $\boldsymbol{n}$ is the unit normal (into the liquid) and $\boldsymbol{t}$ is the unit tangent (in the transverse plane and direction of increasing z^*) to the meniscus. In the normal stress balance, we assume that the transverse temperature variations are small enough (ensured via a small transverse Capillary number introduced later in this section) such that the Young–Laplace equation holds and the meniscus is a circular arc.

For thermal boundary conditions on the solid portions of the boundaries, we consider the cases of heating from the SHS and heating from the solid top wall separately. When heating from the SHS, we have a constant heat flux on the ridge tips and the solid wall is insulated [14, 15]:

$$-k \frac{\partial \theta^*}{\partial y^*} = q_{\mathrm{sl}}'' \quad \text{for } y^* = 0 \text{ and } z^* \in [a^*,\, d^*], \tag{4a}$$

$$\frac{\partial \theta^*}{\partial y^*} = 0 \quad \text{for } y^* = h^* \text{ and } z^* \in [0,\, d^*], \tag{4b}$$

where k is the thermal conductivity and q_{sl}'' is the heat flux per unit area. When heating from the solid wall, the ridge tips are insulated, and we have a constant heat flux on the solid wall:

$$\frac{\partial \theta^*}{\partial y^*} = 0 \quad \text{for } y^* = 0 \text{ and } z^* \in [a^*,\, d^*], \tag{5a}$$

$$k\frac{\partial \theta^*}{\partial y^*} = q''_{\text{sl}} \quad \text{for } y^* = h^* \text{ and } z^* \in [0,\, d^*]. \tag{5b}$$

Importantly, we note that even though we have used the same symbol q''_{sl} for the two cases (heating via the SHS or solid wall), in general they will take different values. Indeed, later when we compare the two cases, we fix the heat rate (in Watts) through one (half) period to be the same. The heat *rate* is $q''_{\text{sl}}(d^* - a^*)$ when heating via the SHS and $q''_{\text{sl}}d^*$ when heating via the solid wall.

Lastly, we have symmetry conditions on the centreline of the ridges, $y^* \in [0,\, h^*]$ and $z^* = 0$ or $z^* = d^*$, given by

$$\frac{\partial u^*}{\partial z^*} = \frac{\partial v^*}{\partial z^*} = \frac{\partial p^*}{\partial z^*} = \frac{\partial \theta^*}{\partial z^*} = w^* = 0. \tag{6}$$

By considering an energy balance on a control volume of cross-section $\mathcal{A}^* = \{y^* \in [0,\, h^*]\} \times \{z^* \in [0,\, d^*]\}$ with depth $\mathrm{d}x^*$, the fully-developed assumption implies that $\partial\theta^*/\partial x^*$ is a constant. This means that θ^* increases linearly with x^* and the axial diffusion term in (1) is zero [27]. When we heat from the SHS, we have

$$\frac{\partial \theta^*}{\partial x^*} = \frac{2\alpha q''_{\text{sl}}(d^* - a^*)}{kQ^*}, \tag{7}$$

and when we heat from the solid wall,

$$\frac{\partial \theta^*}{\partial x^*} = \frac{2\alpha q''_{\text{sl}} d^*}{kQ^*}, \tag{8}$$

where $Q^* = \iint_{\mathcal{A}^*} u^* \mathrm{d}\mathcal{A}^*$ is the volumetric flow rate in the x^* direction per period.

2.2 Model assumptions

The problem as stated has a three-dimensional velocity field coupled to a three-dimensional temperature field via the tangential stresses, and hence comprises a formidable nonlinear boundary-value problem. Following [13], we define the cross-plane Reynolds number as $Re_\perp = \rho\gamma|q''_{\text{sl}}|{a^*}^2/(\mu^2 k)$, which represents the balance between the velocities (inertia) that arise solely due to TCS and viscous stresses. Assuming $Re_\perp \ll 1$, the inertial terms are negligible and u^* decouples from v^* and w^* in (1). This retains the streamwise TCS on the meniscus, whilst eliminating v^* and w^* from the calculation of the total thermal resistance. One can also define the transverse Capillary number $Ca_\perp = \gamma|q''_{\text{sl}}|a^*/(\sigma_0 k)$, which represents the balance between transverse velocities and surface tension. Under the assumption $Ca_\perp \ll 1$, it can be shown that one can retain the effects of TCS in the tangential stress without violating the circular arc assumption [13]. We will address the validity of some of these assumptions (e.g. $Re_\perp \ll 1$) in Sec. 5.5, where we compare our model predictions with numerical simulations.

2.3 Non-dimensionalisation

With these simplifications, non-dimensionalising the velocity using the typical pressure-driven velocity scale ($U^* = d^{*2}(-\partial p^*/\partial x^*)/(2\mu)$) and lengths with d^*, the streamwise momentum equation transforms to

$$\nabla_\perp^2 u = -2, \tag{9}$$

subject to

$$\boldsymbol{n}\cdot\boldsymbol{\nabla} u = \frac{A}{Q} \quad \text{for } y \in \mathcal{S} \text{ and } z \in [0,\, \delta], \tag{10a}$$

$$u = 0 \quad \text{for } y = 0 \text{ and } z \in [\delta,\, 1], \tag{10b}$$

$$u = 0 \quad \text{for } y = h \text{ and } z \in [0,\, 1], \tag{10c}$$

$$\frac{\partial u}{\partial z} = 0 \quad \text{for } y \in [0,\, h] \text{ and } z = 0, 1, \tag{10d}$$

where $\delta = a^*/d^*$ is the cavity or slip fraction, and $h = h^*/d^*$ is the channel height. When we heat from the SHS,

$$A = \frac{4\mu\gamma\alpha q''_{\text{sl}}(d^* - a^*)}{k{d^*}^5(\partial p^*/\partial x^*)^2}, \tag{11}$$

and when we heat from the solid wall,

$$A = \frac{4\mu\gamma\alpha q''_{\text{sl}}}{k{d^*}^4(\partial p^*/\partial x^*)^2}, \tag{12}$$

where A is a constant representing the strength of the streamwise TCS. These two definitions of A coincide exactly if the heat rate, which is $q''_{\text{sl}}(d^* - a^*)$ in (11) and $q''_{\text{sl}}d^*$ in (12), is made the same (and thus the heat flux q''_{sl} will necessarily take different values). This is to be expected because A originates from a thermal energy balance and depends only on the total heat energy entering the domain. Thus, fixing the same value of A in both cases can be viewed, given the same fluid and geometry, as fixing the heat rate. When directly comparing the two heating configurations in section 5.4 for an electronics cooling application, choosing the same value of A is necessary for a fair comparison.

The other tangential stress balance which couples the velocity to the temperature field involves only wall normal and transverse velocities and therefore is not needed in our analysis.

We non-dimensionalise the temperature field using $\theta = (\theta^* - \theta^*_{\text{m}})k/(q''_{\text{sl}}d^*)$, where θ^*_{m} is the mixed-mean temperature, $\theta^*_{\text{m}} = \iint_{\mathcal{A}^*} u^*\theta^*\mathrm{d}\mathcal{A}^*/Q^*$. When heating occurs from the SHS, the problem transforms to

$$\nabla_\perp^2 \theta = \frac{(1-\delta)u}{Q}, \tag{13}$$

subject to

$$\boldsymbol{n}\cdot\boldsymbol{\nabla}\theta = 0 \quad \text{for } y\in\mathcal{S} \text{ and } z\in[0,\,\delta], \tag{14a}$$

$$\frac{\partial\theta}{\partial y} = -1 \quad \text{for } y=0 \text{ and } z\in[\delta,\,1], \tag{14b}$$

$$\frac{\partial\theta}{\partial y} = 0 \quad \text{for } y=h \text{ and } z\in[0,\,1], \tag{14c}$$

$$\frac{\partial\theta}{\partial z} = 0 \quad \text{for } y\in[0,\,h] \text{ and } z=0,\,1. \tag{14d}$$

When heating occurs from the solid wall, the problem transforms to

$$\nabla_\perp^2\theta = \frac{u}{Q}, \tag{15}$$

subject to

$$\boldsymbol{n}\cdot\boldsymbol{\nabla}\theta = 0 \quad \text{for } y\in\mathcal{S} \text{ and } z\in[0,\,\delta], \tag{16a}$$

$$\frac{\partial\theta}{\partial y} = 0 \quad \text{for } y=0 \text{ and } z\in[\delta,\,1], \tag{16b}$$

$$\frac{\partial\theta}{\partial y} = 1 \quad \text{for } y=h \text{ and } z\in[0,\,1], \tag{16c}$$

$$\frac{\partial\theta}{\partial z} = 0 \quad \text{for } y\in[0,\,h] \text{ and } z=0,\,1. \tag{16d}$$

The dimensionless domain is similar to the curved meniscus problem studied by [26], where for $z\in[0,\,\delta]$ we can evaluate the shape of the liquid–gas interface as

$$\mathcal{S} = \sqrt{R_\varphi^2-\delta^2}-\sqrt{R_\varphi^2-z^2} \quad \text{if } \varphi>0, \tag{17a}$$

$$\mathcal{S} = \sqrt{R_\varphi^2-z^2}-\sqrt{R_\varphi^2-\delta^2} \quad \text{if } \varphi<0, \tag{17b}$$

where $\varphi=\arcsin(\delta/R_\varphi)$ is the positive or negative protrusion angle and R_φ is the radius of curvature of the meniscus.

The system (9)–(17) comprises the isoflux convection problem, coupling the streamwise velocity and temperature fields via TCS at a curved meniscus, under fully-developed conditions. The system (9)–(17) is valid for any h, δ, φ and A, provided $Re_\perp \ll 1$.

3 Quantities characterising the total thermal resistance

3.1 Flow rate

Before we present and discuss the numerical results of our model, we highlight the global quantities that are of interest in heated channel flows between a SHS and a solid wall. The caloric resistance is inversely proportional to the flow rate Q, and hence we may use Q to quantify the effect on caloric heat transfer. In particular, we investigate the dependence of Q on the slip fraction (δ), protrusion angle (φ), channel height (h) and thermocapillary forcing (A). It is calculated as

$$Q = \int_{z=0}^{\delta}\int_{y=\mathcal{S}}^{h} u\,\mathrm{d}y\mathrm{d}z + \int_{z=\delta}^{1}\int_{y=0}^{h} u\,\mathrm{d}y\mathrm{d}z. \tag{18}$$

3.2 Nusselt number

We will quantify the convective resistance of the heated channel using the Nusselt number, Nu. We use Nu to evaluate the decrease in convective heat transfer (between the solid surface and liquid) due to the implementation of SHSs and investigate its dependence on δ, φ, h and A [26]. When heating occurs from the SHS,

$$Nu = \int_{z=\delta}^{1}\frac{2h\,\mathrm{d}z}{\theta(0,\,z)}, \tag{19}$$

and when heating occurs from the solid lid,

$$Nu = \int_{z=0}^{1}\frac{2h\,\mathrm{d}z}{\theta(h,\,z)}. \tag{20}$$

3.3 Total thermal resistance

In general, the values of δ that minimise the caloric resistance will maximise the convective resistance, and vice versa. However, the total thermal resistance is the relevant quantity to minimise for a physical channel with finite length L^* in the streamwise direction. The total thermal resistance is a weighted sum of the convective and caloric resistances [22]. In dimensional form this quantity is defined to be $R^*=(\bar{\theta}^*_{\text{s,out}}-\theta^*_{\text{m,in}})/((d^*-a^*)q''_{\text{sl}}L^*)$, where $\bar{\theta}^*_{\text{s,out}}$ is the average temperature on the heated surface at $x^*=L^*$ and $\theta^*_{\text{m,in}}$ is the mixed-mean temperature at $x^*=0$. By adding and subtracting the mixed-mean temperature at $x^*=L^*$, this can be decomposed into caloric and convective resistances. When heating via the SHS, R^* is given by

$$R^* = \frac{\alpha}{kQ^*}+\frac{\bar{\theta}^*_{\text{s,out}}-\theta^*_{\text{m,out}}}{(d^*-a^*)q''_{\text{sl}}L^*}, \tag{21}$$

and when heating via the solid surface,

$$R^* = \frac{\alpha}{kQ^*}+\frac{\bar{\theta}^*_{\text{s,out}}-\theta^*_{\text{m,out}}}{d^*q''_{\text{sl}}L^*}. \tag{22}$$

The dimensionless resistance R (scaled using kU^*d^{*2}/α) is then given by

$$R = \frac{1}{Q}+\frac{P\acute{e}}{L(1-\delta)^2}\int_{z=\delta}^{1}\theta(0,\,z)\mathrm{d}z, \tag{23}$$

when heating via the SHS and

$$R = \frac{1}{Q}+\frac{P\acute{e}}{L}\int_{z=0}^{1}\theta(h,\,z)\mathrm{d}z, \tag{24}$$

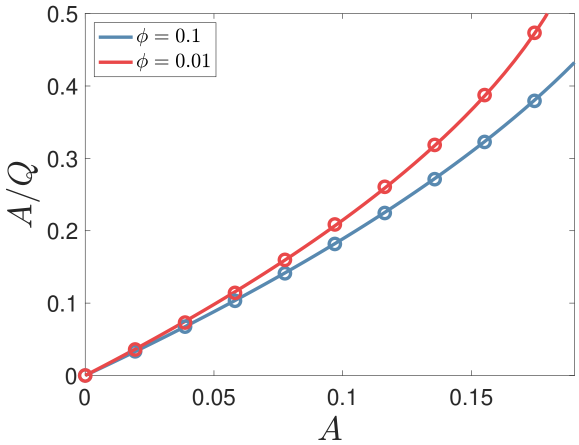

Fig. 2. A comparison between solutions to the TCS problem for different solid fractions ($\phi = 1 - \delta$), using the framework employed herein (given by the solid lines) and the solution to the problem within [9] (given by the symbols).

when heating via the solid surface. Here, $L = L^*/d^*$ is the dimensionless streamwise length of the channel and $P\acute{e} = RePr = U^*d^*/\alpha$ is the Péclet number. The first and second terms in (23)–(24) correspond to the dimensionless caloric and convective resistances, respectively, and indicate how the caloric and convective resistances depend on the flow rate and Nusselt number. We now proceed to maximise (Q, Nu) individually, and then minimise R, with respect to the parameters h, δ, φ, L, and $P\acute{e}$.

4 Numerical methods and algorithm validation

The numerical solution to both problems stated above is undertaken using an extension of the framework presented by our group elsewhere [12]. The methods are efficient and accurate due to their spectral nature and the analytical treatment of triple-point singularities, as we briefly explain next. Firstly, the domain is decomposed into two parts, separated by the vertical line $z = \delta$ through the contact point of the meniscus with the ridge. Continuity of u and θ and their first derivatives is then enforced at the dividing line [28]. Secondly, the irregular domains are transformed into canonical Chebyshev domains. Thirdly, the discontinuous boundary conditions at $z = \delta$ on the SHS are known to introduce integrable stress singularities into the problem. The leading-order local contributions of these singularities are subtracted to produce better behaved problems, and the unknown strength of the singularities is determined as part of the numerical solution by imposing a regularity condition there - see [12].

Unlike the adiabatic problem, in the presence of thermal effects and resulting Marangoni stresses, we see from (10) that the forcing at the meniscus depends non-linearly on the velocity through the reciprocal mass-flux term A/Q. Therefore, an iterative technique must be implemented to obtain a solution. It is known from analytical and computational work by [9] that in the case of a flat meniscus there exist two solution branches as the strength A varies. Importantly, it is also established that no solutions exist beyond a critical value of A, and this property also holds for our computations. The parallel flow steady-state assumption breaks down when A is large enough, and the study of such regimes remains an open challenge. [9] find that one solution branch reduces to that expected for a zero shear stress on the meniscus when the heat flux is switched off (i.e. $A \to 0$). The second branch (a result of a transcritical bifurcation) appears to be less relevant in the sense that it does not produce a physical solution as $A \to 0$. In what follows we focus only on the physical solution branch and in particular extend previous work to arbitrary meniscus curvatures that are expected in applications.

The code was validated by comparisons with solutions from [20, 26] in the case $A = 0$, i.e., we ensure that the flow rate and Nusselt number match numerical results from [20] and asymptotic results from [26], when there are no streamwise TCS. Hence, as the main extension of our model is for $A \neq 0$, we validated our solutions with an example provided by [9] for a flat meniscus, i.e. $\varphi = 0$. For convenience, we compare to their asymptotic solution for large channel heights $h \gg 1$; however, the difference from the exact solution is negligible for the parameters chosen here. The only notable difference relevant to the comparisons is that in our work we use d^* to non-dimensionalise lengths rather than $2d^*$ used in [9]. Following [9] we examine the variation of thermocapillary ratio A/Q on A for different solid fractions $\phi = 1 - \delta$. Results are given in Fig. 2 for $\phi = 0.01$ to $\phi = 0.1$ with solid lines depicting our simulations and open circles the results of [9]. Our numerical framework attains the positive (lower) branch of this solution and agreement is excellent. This inability to converge to the other solution is also the case in the direct numerical simulations carried out within [9].

A final validation of our model is presented in Sec. 5.5, where we compare our model to numerical simulations performed in ANSYS FLUENT, including meniscus curvature and both streamwise and transverse TCS. In terms of run time, the model takes seconds to solve (9)–(17) on a laptop computer, whereas, ANYS FLUENT takes days to solve (1)–(8) on a computer cluster. The memory requirements are also significantly less, as the model solves (9)–(17) for 2 variables in 2D space and ANYS FLUENT solves (1)–(8) for 5 variables in 3D space. This means that extensive parameter studies to find optimal geometries are possible when solving the model but not when solving the full equations.

5 Results and discussion

5.1 Flow rate

We begin our analysis by examining the caloric resistance through the normalised flow rate, $\widehat{Q} = Q/Q_{\mathrm{B}}$, where Q has been defined in (18) and Q_{B} is the volumetric flow rate for a smooth-walled channel over a unit transverse interval (the Q_{B} is a known classical result for pressure-driven flows). Note that for both the heated SHS and solid wall problems the flow rate is identical, and therefore, we consider both cases as one. The value of $\widehat{Q}$ represents the in-

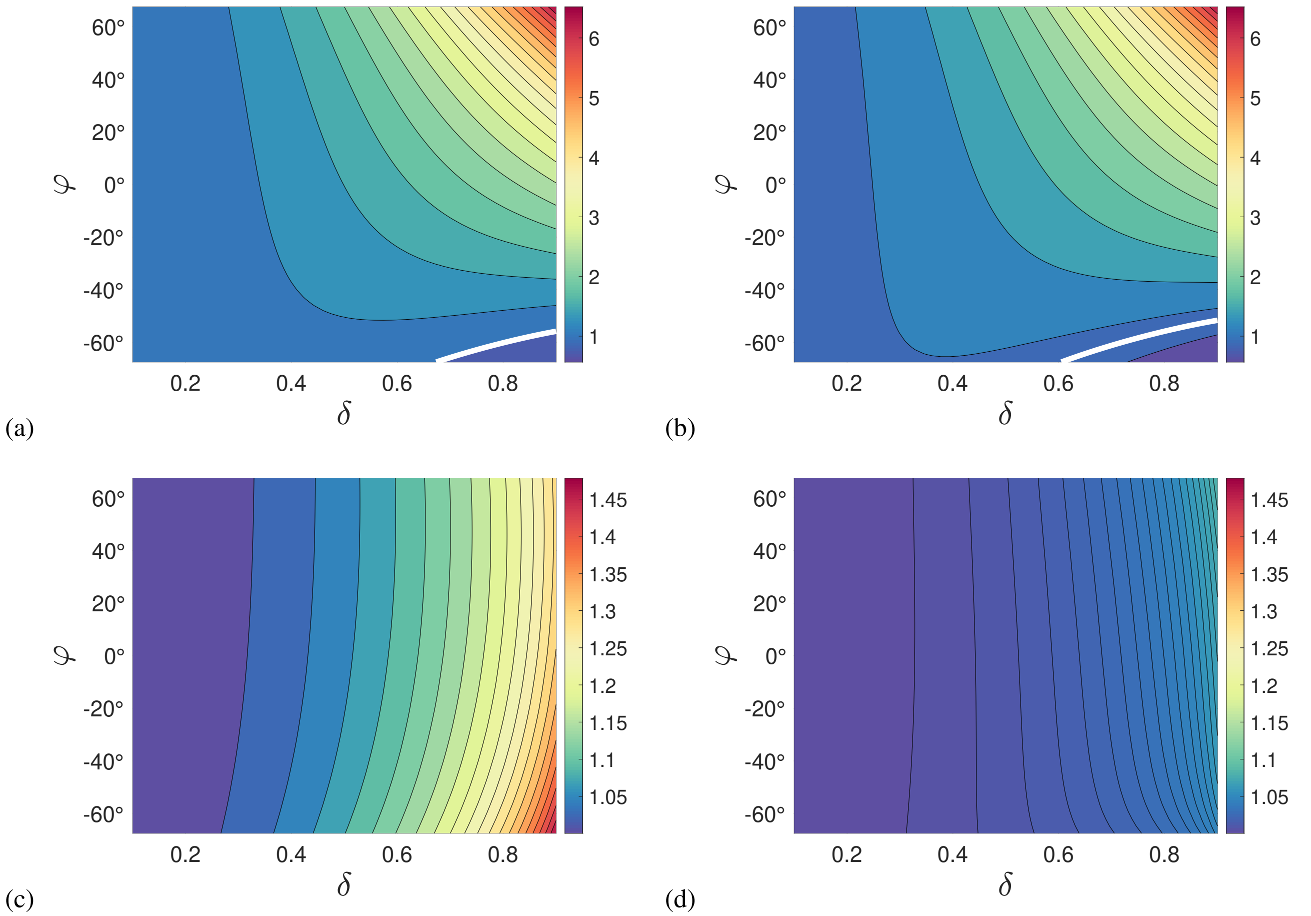

Fig. 3. Contours demonstrating the normalised flow rate's ($\widehat{Q}$) dependence on the slip fraction (δ) and protrusion angle (φ) when heating from the SHS, where $\varphi > 0$ indicates deflection into the gas cavity. We vary the channel height from $h = 1$ (a) $A = 0$ and (b) $A = 0.02$, to $h = 10$ (c) $A = 0$ and (d) $A = 1.4$, where A is the streamwise thermocapillary stress.

crease in flux due to the implementation of SHSs for a given geometry, and the limits $h \to \infty$ or $\delta \to 0$ yield $\widehat{Q} \to 1$. A range of protrusion angles φ and slip fractions δ can be achieved via the implementation of different fluid species in the channel and cavity [21]. One must also examine the effects of h and A on bulk flow phenomena, as we detail next.

We consider the effect of the slip fraction δ, the protrusion angle φ, and the streamwise thermocapillary stress A on the normalised flow rate $\widehat{Q}$. Results are shown for two channel heights $h = 1$ and $h = 10$ in Fig. 3. For each configuration, our numerical solution exists for a finite range of A, δ and φ, as found in the flat meniscus case [9]. To fix matters, we took $\delta \in [0.1, 0.9]$, $\varphi \in [-67.5°, 67.5°]$, and carried out computations up to the maximum possible streamwise thermocapillary stress $A = A_{max}$, say, for which solutions can be attained for all values of δ and φ in the chosen intervals. The reason we took these intervals was that extreme values of δ and φ meant that the range of A was diminished. Contour plots are shown that represent the magnitude of $\widehat{Q}$ in the $\delta{-}\varphi$ plane. Panels 3(a)-(b) have $h = 1$, while panels 3(c)-(d) correspond to relatively large heights $h = 10$. When $h = 1$, a solution exists for $A \lessapprox 0.02$, and Figs. 3(a)-(b) depict $\widehat{Q}$ for $A = 0, 0.02$, respectively. For the large height $h = 10$, we find existence of solutions for $A \lessapprox 1.4$, and present results for $A = 0, 1.4$ in panels 3(c)-(d), respectively. For these results, and guided by applications, we only consider $A \geq 0$, corresponding to a heat flux into the liquid (or none at all).

For $h = 1$ and in the absence of TCS, $A = 0$, Fig. 3(a) shows that $\widehat{Q}$ increases as δ increases and φ becomes large and positive. For a fixed δ, $\widehat{Q}$ increases monotonically with φ. For fixed large and negative φ (i.e. menisci protruding into the liquid), a local maximum is attained for a given δ; otherwise $\widehat{Q}$ increases with increasing δ. Allowing TCS with $A = 0.02$ predicts the same general trends as seen in Fig. 3(b). Importantly, however, the magnitude of $\widehat{Q}$ has decreased for all φ and δ, heralding the adverse effect of TCS on the thermal management of superhydrophobic channels. In both these configurations we encounter $\widehat{Q} < 1$, implying that here one would be better off not implementing SHSs. The thick white curve depicts the boundary $\widehat{Q} = 1$, and can be seen in Fig. 3(a)-(b) in the bottom right corner (large δ and large negative φ) when $A = 0$. This behaviour is amplified as A continues to grow, as Fig. 3(b) shows that $\widehat{Q}$ becomes less than unity for a slightly wider range of δ.

Results for larger channel heights $h = 10$ are shown in panels 3(c)-(d), and less variation in $\widehat{Q}$ is seen compared

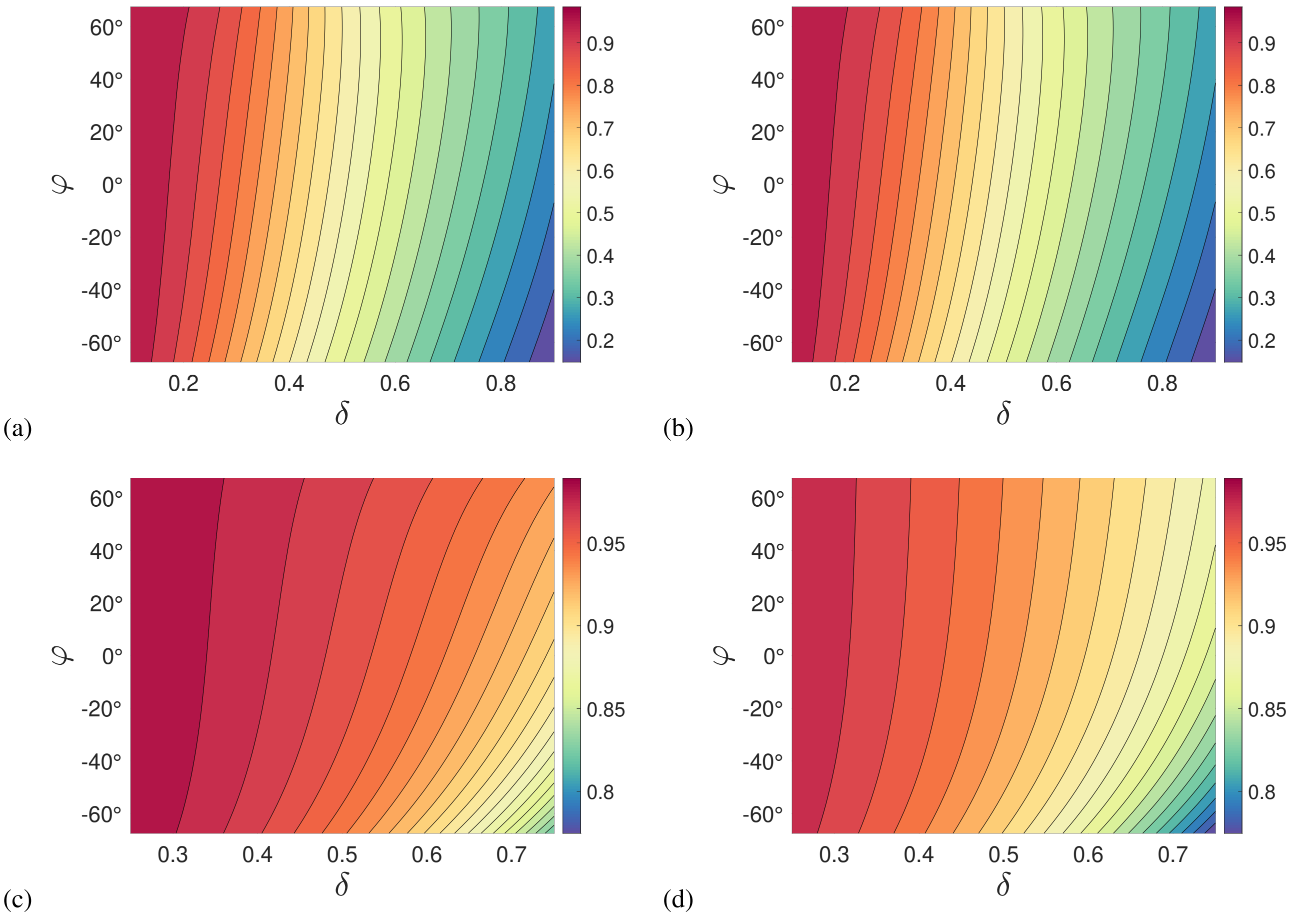

Fig. 4. Contours demonstrating the normalised Nusselt number's ($\widehat{Nu}$) dependence on the slip fraction (δ) and protrusion angle (φ) when heating from the SHS, where $\varphi > 0$ indicates deflection into the gas cavity. We vary the channel height from $h = 1$ (a) $A = 0$ and (b) $A = 0.02$, to $h = 10$ (c) $A = 0$ and (d) $A = 1.4$, where A is the streamwise thermocapillary stress.

to the $h = 1$ case in panels 3(a)-(d). In addition, the solution exists for a larger range of thermocapillary stresses, $A \lessapprox 1.4$. When $A = 0$, the main difference for larger h is the monotonic increase of $\widehat{Q}$ with increasing δ and decreasing φ. There also exists a minimum of $\widehat{Q}$ as φ varies for fixed large δ. As A increases to 1.4, the trends of panel 3(c) persist in panel 3(d) with respect to δ, however, $\widehat{Q}$ now increases with increasing φ (as was the case when $h = 1$ in 3(b)). These results show that the larger TCS induces a further reduction in $\widehat{Q}$ and hence exacerbates the reduction in flow rate relative to smooth-walled channels. Physically, for panels 3(c)-(d), the TCSs at the meniscus are not large enough to overcome the benefits of slip induced by the gas phase, implying that all SHS configurations increase the volumetric flow rate. Therefore, $\widehat{Q}$ is maximised for channels with SHSs and as $\delta \to 1$.

5.2 Nusselt number

With $\widehat{Q}$ analysed, we next examine the convective resistance through the normalised Nusselt number, $\widehat{Nu} = Nu/Nu_{\mathrm{B}}$, which is the ratio of Nu from (19) with that attained for a smooth-walled channel, Nu_{B}. The quantity $\widehat{Nu}$ represents the change in heat transfer due to the implementation of SHSs when compared to smooth walls, where as $\delta \to 0$ or $h \to \infty$ we have $\widehat{Nu} \to 1$. Note that in the case where heat enters the channel from the solid wall, $\widehat{Nu} \approx 1$ for all δ and φ, and therefore, we only consider the case where the channel is heated from the SHS. The behaviour of $\widehat{Nu}$ as δ, φ, A and h vary is established next. Due to the coupling of the velocity and temperature fields, the restrictions on the values of A for which steady-states are possible are the same as in Sec. 5.1.

Figs. 4(a)-(b) examine $\widehat{Nu}$, plotted against δ and φ when $h = 1$, for $A = 0$ and 0.02 respectively. When $A = 0$ it follows from Fig. 4(a) that $\widehat{Nu}$ increases with decreasing δ and increasing φ. The smallest convective resistance, for a given SHS, is attained for large meniscus protrusion into the gas cavity. Physically this is reasonable since we are replacing heat conducting solid surface with adiabatic gas-filled cavities. As a result, $\widehat{Nu} < 1$ for all φ and δ considered, such that a smooth surface would be preferable if minimisation of the convective resistance was our sole concern. The variation in the (δ, φ)-plane is much the same in Fig. 4(b) where $A = 0.02$. As A increases we observe that $\widehat{Nu}$ reduces uniformly, implying that streamwise TCSs are detrimental to the

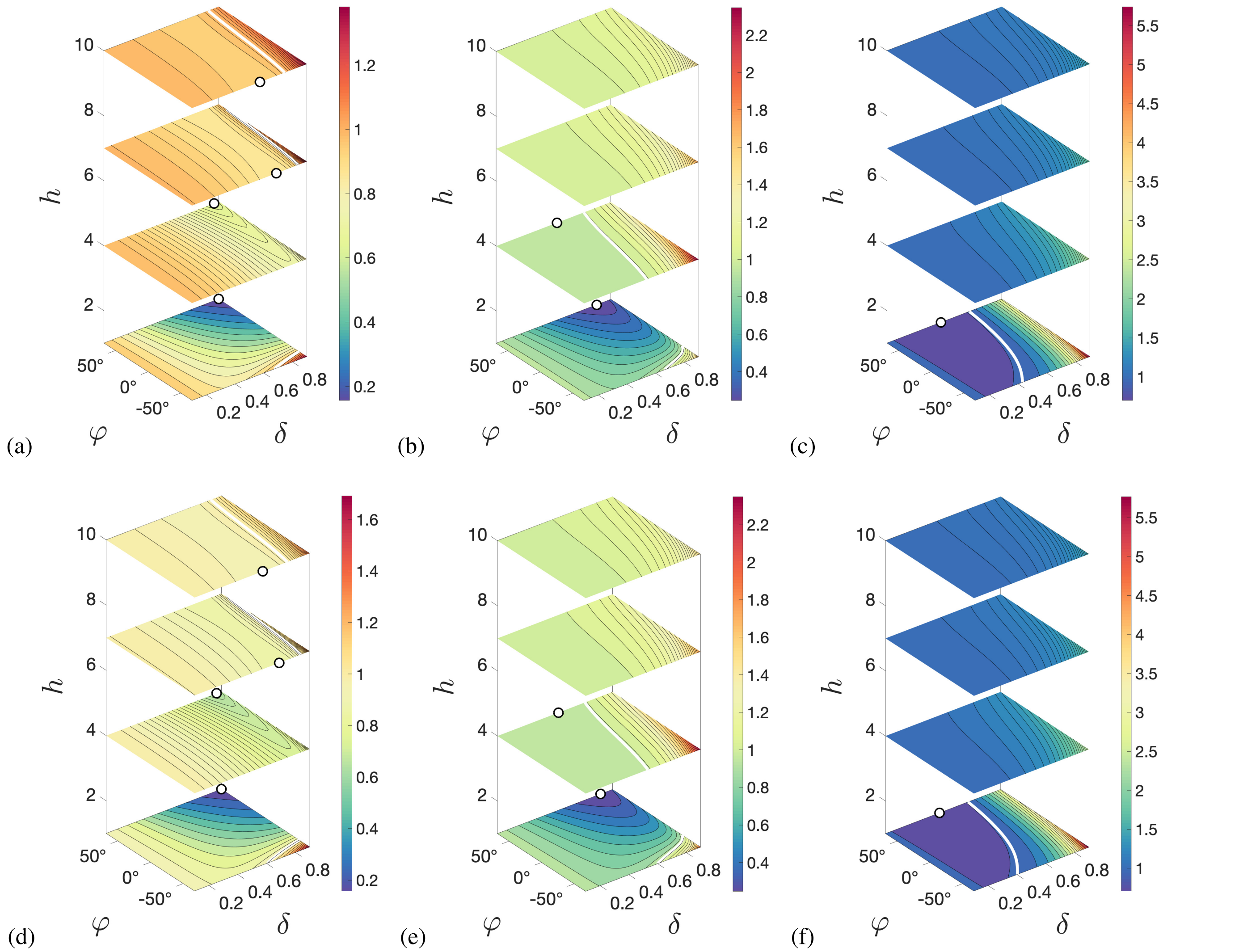

Fig. 5. Contours demonstrating the normalised total thermal resistance's $(\widehat{R})$ dependence on the slip fraction (δ), protrusion angle (φ) and channel height (h) when heating from the SHS, where $\varphi > 0$ indicates deflection into the gas cavity. We vary the streamwise thermocapillary stress from $A = 0$ (a) $\Gamma = 0.0001$, (b) $\Gamma = 0.01$ and (c) $\Gamma = 1$, to $A = 0.02h^3$ (d) $\Gamma = 0.0001$, (e) $\Gamma = 0.01$ and (f) $\Gamma = 1$, where $\Gamma = P\acute{e}/L$, $P\acute{e}$ is the Péclet number and L is the streamwise length of the channel. Here, the white dot represents the minimum and the white line specifies where $\widehat{R} = 1$. If the white dot is not visible, this means that solid walls are preferable to SHSs for heat transfer.

heat transfer from the ridge to the liquid. In summary, we can conclude that regardless of the liquid–gas protrusion angle, the smaller the δ and A the greater the improvements in heat transfer in the presence of SHSs. This variation with δ, where low values are favoured, is the opposite to that seen for the flow rate, where large values of δ are favoured. A balance between these opposing behaviours will then be struck by the consideration of the total thermal resistance in Sec. 5.3. Increasing A, however, is detrimental to both the heat transfer and flow rate.

When we increase the channel height to $h = 10$ (see Figs. 4(c)-(d)), it remains the case that $\widehat{Nu}$ is maximised by small δ and large φ. Compared to the case when $h = 1$, we find that the range of $\widehat{Nu}$ values attained is much smaller and closer to one (in a similar manner to $\widehat{Q}$). Furthermore, the increases in A have much less of an effect on $\widehat{Nu}$ than we saw for $\widehat{Q}$. In summary, for all A considered, heat transfer is at its most efficient for small δ and large $\varphi > 0°$. This is again in direct opposition to the configurations that optimise the flow rate $\widehat{Q}$ in §5.1.

5.3 Total thermal resistance

We now consider an optimisation of the flow geometry taking into account the finite streamwise extent of the channel. To apply SHSs to the cooling of mechanical and electrical components, one wishes to maximise both the volumetric flow rate $\widehat{Q}$ and Nusselt number $\widehat{Nu}$, since both quantities independently contribute to the total thermal resistance R defined in equation (23) for a finite length of channel [22]. The results of Sec. 5.1 and 5.2, indicate that the geometries which enhance $\widehat{Q}$ and $\widehat{Nu}$ are vastly different when heating occurs from the SHS. Therefore, we must examine the balance between varying the channel length and Péclet number to minimise the total thermal resistance. The streamwise variation has been removed from our analysis due to the fully developed assumption, however, the streamwise dimension needs to be taken into account in order to optimise the full 3D problem [20]. We consider the normalised value of the total thermal resistance, $\widehat{R} = R/R_{\mathrm{B}}$, where R_{B} is the corresponding value for smooth-walled channels, i.e. $\delta = 0$. This measure represents the improvements due to SHSs for a given flow configuration, operating parameters (heat rate through one period and pressure gradient), liquid properties and channel geometry. When heating occurs from the solid wall, changes in δ and φ have a very small effect on the convective resistance, and therefore, the geometry which maximises the caloric resistance also maximises the total thermal resistance. Hence, we do not need to calculate $\widehat{R}$ in this case, as the optimal geometries are the same as those which maximised $\widehat{Q}$ in Sec. 5.1. Instead, we compare $\widehat{R}$ when heating occurs from the SHS and solid wall in Sec. 5.4, using parameters characteristic of microchannel applications. We will focus in this section on the case where heat enters via the SHS.

Considering the expression for $\widehat{R}$ in (23), it is clear that we wish to increase L and decrease $P\acute{e}$ in order to minimise $\widehat{R}$. The former effect allows for a greater heat transfer due to heat dissipation over a larger L, and the latter increases the diffusive transport rate (and depends on the liquid that we are considering). To quantify this more directly, we introduce the ratio $\Gamma = P\acute{e}/L$, which we will use to summarise the results presented in a given figure. To reduce the Péclet number one could employ a liquid metal, which has a lower Prandtl number (Pr) and has been demonstrated to be beneficial in SHS channel flows previously [21]. We wish to examine a wide range of A, $P\acute{e}$, L, h, δ and φ, to attain an understanding of the liquid and geometries which reduce $\widehat{R}$ by the greatest amount. To this end we present our computations in three-dimensional plots depicting values of $\widehat{R}$ against δ, φ and h for fixed values of A, $P\acute{e}$ and L. Note that $\widehat{R}$ is a quantity that depends on integrals over the domain, so each point in the 3D plots corresponds to a distinct computation.

In Figs. 5(a)-(c) and 5(d)-(f) we compute $\widehat{R}$ for different h, L and $P\acute{e}$, with $A = 0$ in the former and $A = 0.02h^3$ in the latter set of results respectively. Results are ordered for increasing Γ and it can be seen from its definition that the corresponding values of $P\acute{e}$ and L are not necessarily monotonic as we move through the panels. The colour bar indicates the value of $\widehat{R}$ and inspection of the plots for any given height h immediately predicts whether a given φ and δ results in an increase ($\widehat{R} > 1$, colour-coded towards darker red) or decrease ($\widehat{R} < 1$, colour-coded towards darker blue) of the thermal resistance. The global minimum of $\widehat{R}$ over all computed φ, δ for a given h, is in turn determined and identified with a white circle in the plots. These circles denote the desired optimal values for a given parameter set. In what follows we structure the results by describing the effects on the thermal resistance for small Γ, intermediate Γ (that inherits phenomena from the extreme cases), and finally, large Γ.

Beginning with 5(a), namely $A = 0$, $P\acute{e} = 0.01$ and $L = 100$, we observe first that in all cases $\widehat{R} < 1$ for a given δ and φ, so that SHSs are favoured so long as they're designed appropriately. In addition, the optimal solution occurs at a slip fraction which is dependent on h, with higher channels favouring menisci protruding into the liquid ($\varphi \approx -67.5°$), while at smaller heights $h < 7$ optimal thermal resistances are achieved for menisci protruding into the gas with $\varphi \approx 67.5°$.

In panel 5(b) we increase Γ by a factor of a hundred by keeping $L = 100$ but increasing $P\acute{e}$ to 10. The trends are similar to panel 5(a) but with three notable differences: (i) $\widehat{R}$ is no longer less than unity for all h (we return to this below); (ii) optimal solutions with menisci protruding into the liquid are no longer attained; (iii) optimal solutions occur for smaller values of δ, with δ decreasing as h increases (for example, we find optimal $\delta \approx 0.5$ for $h = 4$). Regarding point (i) above, we note that with the exception of $h = 7 - 10$, all configurations in panel 5(b) yield $\widehat{R} < 1$ for a given δ and φ. In the cases $h = 1$ to $h = 4$, some regions of the $\varphi - \delta$ plane have $\widehat{R} > 1$, and we have plotted a white curve to denote the boundary when $\widehat{R} = 1$. For these values of h there are regions in parameter space to the right of the dividing white curve, where smooth channels would be more beneficial than SHSs.

As Γ increases further, the benefits of SHSs to heat transfer are lost almost completely as seen in panel 5(c). In panel 5(c) where $P\acute{e} = 10$, $L = 10$ ($\Gamma = 1$) we see that for $h = 1$ there are regions in the $(\delta, \varphi)-$plane supporting $\widehat{R} < 1$, but for $h > 1$ all computations show $\widehat{R} > 1$ for all δ and φ. With the exception of the smallest heights where SHSs are favoured, all optimal solutions occur for the smallest available δ and with menisci protruding into the gas cavity. These results show that maximisation of $\widehat{Nu}$ with solid walls is preferable to SHSs, i.e. the caloric resistance dominates in the calculation of the total thermal resistance.

Next we consider a non-zero thermocapillary stress with $A = 0.02h^3$ (this represents the maximum A for which we could compute converged solutions across all parameters presented for a given h). We know from §5.1-5.2 that increasing A results in a decrease in both $\widehat{Q}$ and $\widehat{Nu}$, suggesting that $\widehat{R}$ will also be larger. However, the location of the minimum may differ and hence requires investigation. The other parameters in Fig. 5(d)-(f) are identical to those in Fig. 5(a)-(c) and the results are similar to the $A = 0$ case. The main difference is an overall increase in $\widehat{R}$ in all cases, as anticipated, while the progression of the optimal solution as h is increased for each Γ, is analogous to that in Fig. 5(a)-(c). The attained ranges of $\widehat{R}$ in each panel are reduced for increasing A. We can conclude, therefore, that the presence of TCS increases the thermal resistance and is detrimental to thermal management goals. Examining the evolution of Γ from 0.0001 to 1 in Fig. 5(d)-(f), the three regimes described when $A = 0$ occur and we have that TCSs reduce the range of $\widehat{R}$ and SHSs are beneficial for a smaller range of Γ.

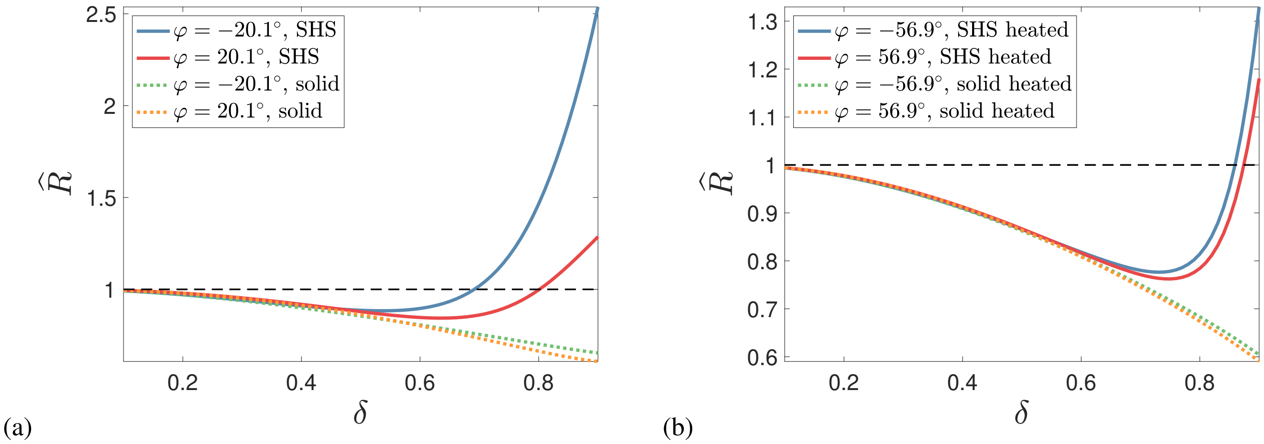

Fig. 6. The total thermal resistance ($\widehat{R}$) characteristic of microchannel applications for different slip fractions (δ) and different protrusion angles (φ) when the channel is heated from the SHS (solid lines) and solid wall (dashed lines) for (a) water and (b) Galinstan, where $\varphi > 0$ indicates deflection into the gas cavity

5.4 Applications

We now consider microchannel configurations characteristic of applications in thermal management of electronics, with both water and Galinstan as the working liquid. Galinstan, a liquid metal, has previously been shown to be advantageous in the application of SHSs to the thermal management of electronics [9,13,22]. We fix the channel height $h^* = 40\ \mu$m and period $d^* = 10\ \mu$m, such that slip fractions from $0.1 \leq \delta \leq 0.9$ are considered. There exists a maximum pressure gradient, $(\partial p^*/\partial x^*)_{max}$, where the liquid remains suspended in the Cassie-Baxter state at the inlet, for a channel that is 1 cm long. Here, the pressure difference across the meniscus is highest and it reduces as one progresses down the length of the channel as the internal pressure decreases [10]. Following [22], we have $(\partial p^*/\partial x^*)_{max} = \sigma\cos(\pi - \varphi_A)/(a^* L^*)$, where σ is the surface tension, φ_A is the advancing protrusion angle and L^* is the channel section length. We assume a canonical average heat flux of 25 Wcm^{-2}, corresponding to a typical value in traditional electronics cooling [8,29]. This corresponds to a heat rate through one (half) period to be $d^* \times 25$ Wcm^{-2} $= 2.5 \times 10^{-5}$ Wcm^{-1}, which we set to be the same for the two heating scenarios to allow a fair comparison. This means that the resulting value of A for the two heating scenarios is the same for a given fluid. The thermophysical properties are taken from [22,30,31].

In Fig. 6(a) we examine the normalised total thermal resistance for water, which has a maximum protrusion angle of $\varphi_A = 20.1°$ [23]. We compare the cases where heat enters the channel from the SHS (solid lines) and solid wall (dashed lines), for angles $\varphi = \pm 20.1°$. For $\delta \lessapprox 0.5$ all curves collapse, such that channels that minimise the caloric resistance dominate the total thermal resistance. As δ increases, the convective resistance effects those curves where the heating occurs from the SHS, such that $\widehat{R}$ hits a minimum for a given δ and then increases. When heating occurs from the solid wall and the other channel wall is textured with a SHS, $\widehat{R}$ decreases monotonically with δ and channels that minimise the caloric resistance dominate the total thermal resistance. In both cases, a SHS with a liquid–gas interface that points into the gas cavity is optimal for minimising $\widehat{R}$.

In Fig. 6(b) we examine $\widehat{R}$ for Galinstan, which has a maximum protrusion angle of $\varphi_A = 56.9°$ [23], significantly larger than that of water. Compared to Fig. 6(a), the total thermal resistance is reduced for all δ and φ, when the channel is heated from either the solid wall or SHS. Employing Galinstan as the internal liquid reduces the effects of the convective resistance (and the detrimental effects of a SHS), meaning that the curves collapse for a larger range of slip fractions, $\delta \lessapprox 0.6$. This also means that those channels where heating occurs through the SHS have $\widehat{R} < 1$ for a greater range of δ. It remains the case, however, that the optimal configuration is heating through the solid wall whilst texturing the other wall with a SHS. In order to maximise the total thermal resistance for thermal management applications, the SHS channel should be designed such that $\delta \to 1$ and $\varphi \to 90°$.

5.5 Comparison with numerical simulations

The above numerical work was done under the assumption of small transverse Reynolds number, defined $Re_\perp = \rho\gamma|q''_{\mathrm{sl}}|a^{*2}/(\mu^2 k)$. It is therefore of interest to understand when this assumption breaks down. To determine this, we ran a series of fully three-dimensional simulations of the general problem (1)–(6) in ANSYS FLUENT, varying $Re_\perp$ from 10^{-1} to 10^4, while holding A constant. These simulations were based on those from [13], and here we will present only on the relevant details and differences.

Since ANSYS FLUENT is a dimensional solver that necessitates a 3D domain for this geometry, we solved a fully 3D version of the dimensional form of the equations (see [13] for more details). The dimensional nature of the solver also meant we needed to input dimensional parameter values to generate our desired dimensionless parameters. To vary $Re_\perp$ independently while keeping A constant, the density ρ and

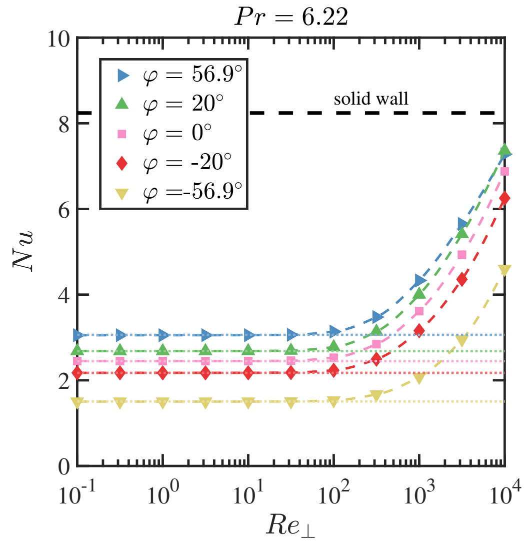

Fig. 7. Nusselt number (Nu) dependence on transverse Reynolds number ($Re_\perp$) for water at various protrusion angles (φ), where $\varphi > 0$ indicates deflection into the gas cavity. The dotted lines are solutions from the small $Re_\perp$ model.

the surface tension γ were modified between each run per the relation $\rho/\gamma = \rho_0/\gamma_0$ where ρ_0 and γ_0 are the actual density and surface tension of the liquid in question, i.e water or Galinstan. This relationship ensured that the group $\gamma\alpha/k$ found in the definition for A remains constant, but the group $\gamma\rho$ found in the definition for $Re_\perp$ increases as γ and ρ increase. We picked $A = 12.8$, which is characteristic of a fairly strong streamwise thermocapillary stress, and is consistent with the examined value of A in [13]. A gas fraction of $\delta = 0.975$ was chosen, motivated by (near) maximal flow enhancement, and also enabling a unique test of the accuracy of the numerical methods outlined in Sec. 4 in a difficult geometry. We considered protrusion angles of 56.9°, 20°, 0° and their negative counterparts. The positive values were selected because they are the maximum for Galinstan [23] and water (on Teflon), respectively.

The two liquids have significantly different Prandtl numbers, $Pr = c_p\mu/k$, with $Pr = 6.22$ for water and $Pr = 0.04$ for Galinstan. Since the Prandtl number is a comparison of momentum diffusivity to thermal diffusivity, the many orders of magnitude difference in the values of this parameters highlights the major difference between the two liquids.

In ANSYS FLUENT, an adaptive mesh protocol was used to allocate more points near the singular triple contact point. A mesh independence study was conducted, resulting in meshes all averaging above 5 million finite volume elements. The solution was considered to be converged when the relative error for a calculated Nusselt number between refinements was less than 10^{-5}. To calculate Nu, the temperature field was extracted from ANSYS FLUENT and imported to MATLAB where quadrature was used to evaluate (19). The calculated values of Nu are plotted against $Re_\perp$ in Fig. 7, for water and all protrusion angles.

Clearly in Fig. 7 there is a convergence to an constant value as $Re_\perp \to 0$, which shows excellent agreement with our model (whose solutions are denoted by short-dashed horizontal lines). Moreover, significant differences between the simulation result and the zero $Re_\perp$ solutions only occurs when $Re_\perp > 10^2$, indicating a fairly large range of validity. However, what is most interesting perhaps is the behaviour of Nu as $Re_\perp$ is increased further. It steadily increases for all angles, nearly approaching that of a parallel-plate channel at $Re_\perp = 10^4$. Moreover, it appears that Nu will continue to increase, and may surpass that of a parallel plate channel under some parameter sets. To physically illustrate why Nu increases with $Re_\perp$, Fig. 8 plots the temperature field for $\phi = 56.9°$ and four different values of $Re_\perp$. The results show that as $Re_\perp$ increases, the temperature field becomes more uniform and temperature gradients are significantly decreased near the ridge—a sign of reduced convective resistance entirely caused by the thermocapillary-induced cross-plane velocity field. Fig. 9 plots this transverse flow for the corresponding cases where the velocities have been normalized by $|\mathbf{u}_\perp|_{\max}$, defined as the maximum speed of the transverse flow when $Re_\perp = 10^4$. It shows that circulation increases considerably as $Re_\perp$ increases, due to larger temperature gradients along the meniscus. Since water has a relatively large Pr number, the advection by the transverse velocity has a large effect. Hotter liquid is advected away from the ridges while colder liquid is brought in from the bulk. This makes the temperature field more uniform, as evident in Fig. 8.

It is worth noting that this increase in Nu does not necessarily mean a decrease in the total thermal resistance, which, as a reminder, is a combination of convective resistance (a function of Nu) and caloric resistance (a function of Q) as seen in (23). In fact, none of our ANSYS FLUENT simulation results show a reduction in the total thermal resistance when compared to a smooth-walled channel. This is because although Nu increased in our simulations, the impact of the caloric resistance on total resistance was affected in two problematic ways, one more physical and one due more to the numerical framework and choice of parameters as we explain next.

First, the more physical one is that the actual caloric resistance rises as $Re_\perp$ grows because thermocapillary mixing slows down the streamwise flow, which can be observed in streamwise velocity field contours in Fig. 10. This is because re-circulation adds a turbulent-like effect to the flow, moving fast moving liquid from the bulk flow towards the ridge. This increases velocity gradients and shear stresses there and, since shear stresses on all walls must still balance the pressure gradient, and the result is a decreased flow rate. Notably, the velocity fields in Fig. 10 become more impacted by the re-circulation at higher $Re_\perp$ than the temperature fields in Fig. 8. This is because $Pr > 1$ for water, meaning momentum diffusion is faster than thermal diffusion. In fact, since $Pr = O(10)$ for water, the temperature field should be affected about one order of magnitude in $Re_\perp$ earlier than the streamwise velocity fields, which can be seen in a comparison of Fig. 8 and Fig. 10.

The second problematic way that the impact of caloric

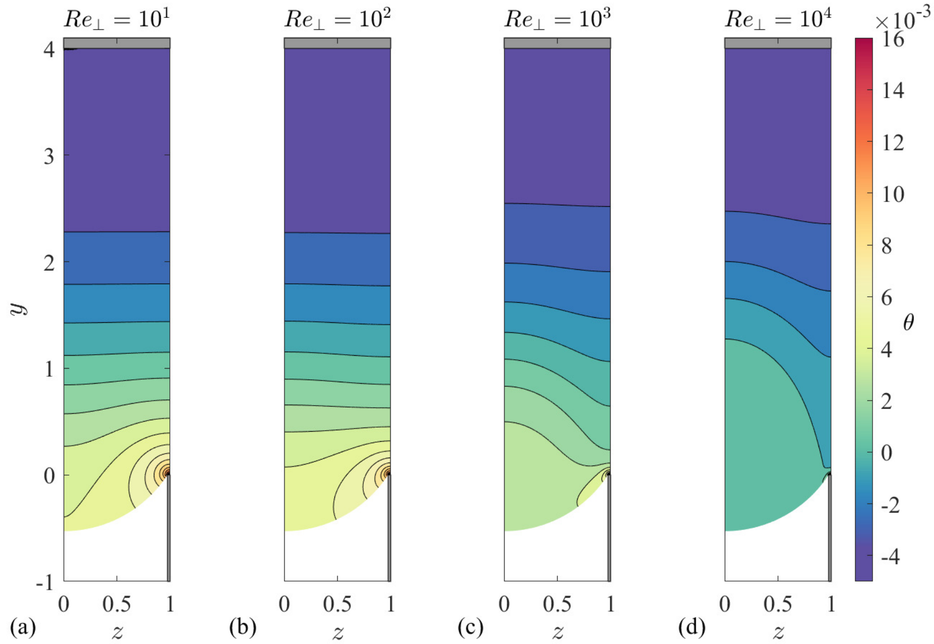

Fig. 8. Temperature (θ) contours of the numerical simulations for water with transverse Reynolds number values (a) $Re_\perp = 10^1$, (b) $Re_\perp = 10^2$, (c) $Re_\perp = 10^3$ and (d) $Re_\perp = 10^4$.

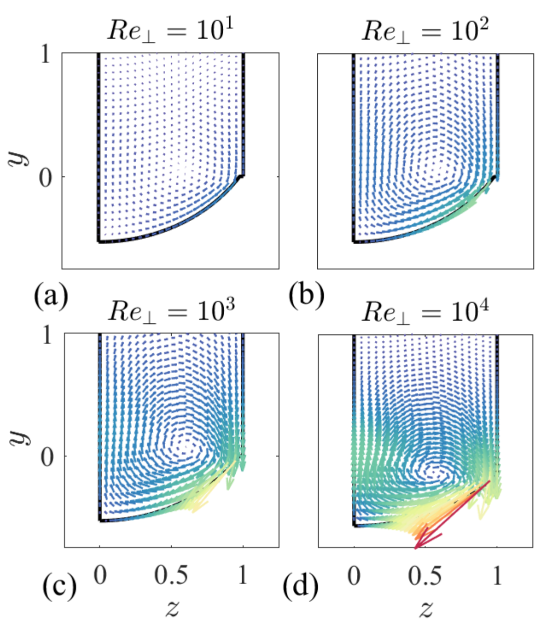

Fig. 9. Vector plots of the cross-plane velocity field $(v,\, w)$, normalised by the maximum speed of the cross-plane velocity when the transverse Reynolds number is $Re_\perp = 10^4$, for (a) $Re_\perp = 10^1$, (b) $Re_\perp = 10^2$, (c) $Re_\perp = 10^3$ and (d) $Re_\perp = 10^4$.

resistance on total resistance is affected as $Re_\perp$ increases is due to our constraint that A be constant for all simulations. By requiring this as $Re_\perp$ increases, $P\acute{e}$ must necessarily increase, leading to a total resistance dominated by the convective resistance as in (23). This means that when $Re_\perp = 10^4$ then $P\acute{e}$ is large and Nu is the only parameter of importance. Then since Nu is still less than the corresponding value for a parallel plate channel, total thermal resistance is not improved. In spite of this, thermocapillary driven mixing does appear to be a mechanism that can increase Nu while simultaneously maintaining some of the lubricating properties of a SHS. We speculate that a different selection of parameters would show both a larger Nu and a larger Q than found in a parallel plate channel, leading to large reductions in the total thermal resistance. We are currently developing a code to test this hypothesis.

The reader may have noticed that results are only presented for water, while Galinstan is omitted. This is because the results are somewhat less interesting. Due the small value of $Pr \approx 0.04$ in the case of Galinstan, the mixing has almost no effect on the temperature fields and, consequently, on Nu. The reason for this is due to the liquid metal nature of Galinstan, implying that the dominant form of heat transfer is conduction, while increased transverse advection has little effect on heat transfer rates. However, the mixing still affects the velocity field by decreasing flow rates. This means that the effect of transverse stresses on the thermal transport using Galinstan is only negative, since an increase in caloric resistance is encountered and at the same time there is no substantive change to convective resistance. The conclusion of our theoretical findings in practical applications, are that large transverse thermocapillary stresses should probably be avoided in systems using Galinstan.

To conclude this discussion about the impact of transverse stresses on heat transfer performance of these systems, it is helpful to calculate realistic values of $Re_\perp$. For the set

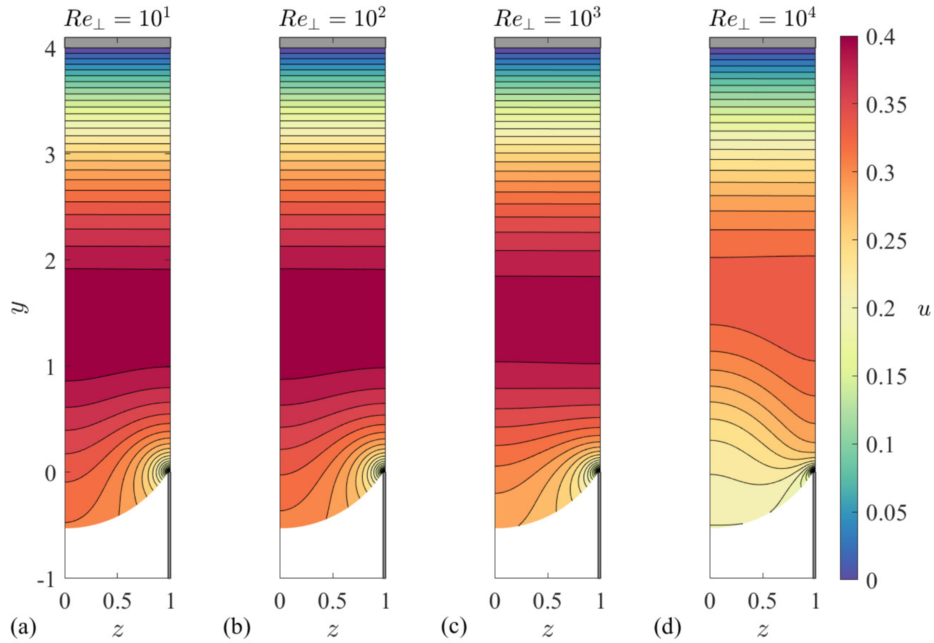

Fig. 10. Streamwise velocity (u) contours for water at constant streamwise TCS (A) for varying transverse Reynolds number (a) $Re_\perp = 10^1$, (b) $Re_\perp = 10^2$, (c) $Re_\perp = 10^3$ and (d) $Re_\perp = 10^4$.

of parameters used in Sec. 5.4 and with $\delta = 0.975$, the values are $Re_\perp \approx 240$ and 76 for water and Galinstan, respectively (thermophysical values for Galinstan were taken from [31]). These numbers are directly on the edge of validity of the zero $Re_\perp$ theory - as evidenced by the results of Fig. 7. However, by simply increasing the pitch d^* from $d^* = 10$ μm to $d^* = 100$ μm these values increase to $Re_\perp \approx 25000$ for water and $Re_\perp \approx 7600$ for Galinstan, due to their dependence on a^{*2}. We also know that $Re_\perp$ increases proportionally to q''_{sl}. As a consequence it appears that whether transverse stresses are important or not depends on the specific system in question, with either scenario possible. Our simulations show that water, due to its larger value of Pr, can outperform Galinstan when transverse stresses are important. Hence, it could be the liquid of choice for systems with long menisci and high heat fluxes. This claim comes with the caveat that water will experience evaporation and condensation along menisci, complicating the multiphysics further, whereas Galinstan will not due to its extremely low vapor pressure. The impact of evaporation and condensation on the heat transfer performance of water is part of ongoing work.

6 Conclusions

In the thermal management of microelectronics, a liquid flow is used to carry heat away from the solid structure to reduce the risk of damage, and the amount of heat carried away is characterised by the total thermal resistance. In this paper, we have investigated the application of superhydrophobic surfaces (SHSs) to the minimisation of the total thermal resistance of a channel, accounting for meniscus curvature and streamwise thermocapillary stress (TCS). When heating occurs from the ridges, SHSs reduce the solid-liquid contact area, which decreases the caloric resistance, but increases the convective resistance. When heating occurs from the opposing solid wall, SHSs reduce the solid-liquid contact area, which decreases the caloric resistance without affecting the convective resistance. For the first time, the optimisation of the total thermal resistance was presented for the following parameters: the slip fraction (δ), the ratio of the channel height to ridge period (h), the meniscus protrusion angle (φ), the TCS strength (A) and the ratio of $P\acute{e}$ to the channel length ($\Gamma = P\acute{e}/L$). Whilst simulation of the full equations with parameters characteristic of microchannel applications is expensive, our reduced model captures much of the physics associated with heated flows over SHSs and allows for inexpensive in-depth parameter studies.

First, we considered the caloric resistance, quantified by the flow rate, and its dependence on channel geometry and streamwise TCS. The flow rate is the same when heating occurs from either the bottom SHS or the opposing solid wall. In general, we found that the flow rate was maximised (caloric resistance minimised) for large slip fractions and menisci protruding into (out of) the cavities for small (large) channel heights. Second, we considered the convective resistance, quantified by the Nusselt number. This only varies with the geometry in the case where heating occurs from the SHS. Our results demonstrated that the Nusselt number is maximised (convective resistance minimised) for large channel heights, small slip fractions, and menisci protruding out of the cavities, and therefore a SHS always exhibits a higher convective resistance than a smooth wall. Third, we investigated the optimisation of the total thermal resistance of a channel with a finite streamwise length where heating occurs from the SHS. The flow rate and Nusselt number both independently contribute to the total thermal resistance. Their relative contributions are controlled by Γ, from which we identify three regimes: (i) $\Gamma = 10^{-4} - 10^{-3}$, caloric-resistance dominated, where maximising the flow rate is most important, and thus SHSs can be optimal; (ii) $\Gamma = 10^{-2} - 10^{-1}$, intermediate region where both resistances are important, with SHSs optimal only for small heights, and a transition to smooth walls optimal at larger heights; (iii) $\Gamma = 1 - 10$, convective resistance dominated, where maximising the Nusselt number is most important, and thus smooth walls are optimal. Increasing the TCS strength results in a decrease in the flow rate, Nusselt number and total thermal resistance.

Finally, we compare both configurations for microchannel cooling applications, where the internal liquid is either water or Galinstan. We demonstrate that it would be considerably better for heating to occur from the solid wall instead of the SHS, and both cases can perform better than a smooth channel. Furthermore, Galinstan reduces the total thermal resistance the most in all cases, where for a fixed channel height, the optimal geometry was found to consist of a SHS with large gas fractions and a liquid–gas interface that protrudes into the gas cavity. We then give a domain of validity to our model by comparing its predictions to simulations of the full equations using ANSYS FLUENT. We identify that the model breaks down due to a cross-plane flow (neglected in our model) that is generated by transverse TCSs. Further modelling is required to reduce the numerical complexity of this problem and predict the total thermal resistance when transverse TCSs are strong.

Acknowledgements

S.D.T. was supported by an EPSRC doctoral scholarship. M.D.M., M.H. and D.T.P. were supported in part by a CBET–EPSRC grant (EPSRC Ref. EP/T030739/1, NSF #2054894). Additionally, we acknowledge discussions with Dr. Georgios Karamanis about the numerical model.

References

[1] Rothstein, J. P., 2010. "Slip on superhydrophobic surfaces". *Annu. Rev. Fluid Mech.,* **42**, pp. 89–109.

[2] Cassie, A. B. D., and Baxter, S., 1944. "Wettability of porous surfaces". *Trans. Faraday Soc.,* **40**, pp. 546–551.

[3] Golovin, K. B., Gose, J. W., Perlin, M., Ceccio, S. L., and Tuteja, A., 2016. "Bioinspired surfaces for turbulent drag reduction". *Philos. Trans. R. Soc. Lond. A,* **374**(2073).

[4] Lee, C., Choi, C., and Kim, C., 2016. "Superhydrophobic drag reduction in laminar flows: a critical review". *Exp. Fluids,* **57**(12), p. 176.

[5] Teo, C. J., and Khoo, B. C., 2009. "Analysis of stokes flow in microchannels with superhydrophobic surfaces containing a periodic array of micro-grooves". *Microfluid. Nanofluidics,* **7**(3), p. 353.

[6] Steinberger, A., Cottin-Bizonne, C., Kleimann, P., and Charlaix, E., 2007. "High friction on a bubble mattress". *Nat. Mater.,* **6**(9), pp. 665–668.

[7] Tsai, P., Peters, A. M., Pirat, C., Wessling, M., Lammertink, R. G. H., and Lohse, D., 2009. "Quantifying effective slip length over micropatterned hydrophobic surfaces". *Phys. Fluids,* **21**(11), p. 112002.

[8] Tuckerman, D. B., and Pease, R. F. W., 1981. "High-performance heat sinking for vlsi". *IEEE Electron device lett.,* **2**(5), pp. 126–129.

[9] Hodes, M., Kirk, T. L., Karamanis, G., and MacLachlan, S., 2017. "Effect of thermocapillary stress on slip length for a channel textured with parallel ridges". *J. Fluid Mech.,* **814**, pp. 301–324.

[10] Game, S. E., Hodes, M., and Papageorgiou, D. T., 2019. "Effects of slowly varying meniscus curvature on internal flows in the cassie state". *J. Fluid Mech.,* **872**, pp. 272–307.

[11] Hodes, M., Lam, L. S., Cowley, A., Enright, R., and MacLachlan, S., 2015. "Effect of evaporation and condensation at menisci on apparent thermal slip". *J. Heat Transfer,* **137**(7), p. 071502.

[12] Game, S. E., Hodes, M., Keaveny, E. E., and Papageorgiou, D. T., 2017. "Physical mechanisms relevant to flow resistance in textured microchannels". *Phys. Rev. Fluid,* **2**(9), p. 094102.

[13] Kirk, T. L., Karamanis, G., Crowdy, D. G., and Hodes, M., 2020. "Thermocapillary stress and meniscus curvature effects on slip lengths in ridged microchannels". *J. Fluid Mech.,* **894**.

[14] Enright, R., Hodes, M., Salamon, T., and Muzychka, Y., 2014. "Isoflux nusselt number and slip length formulae for superhydrophobic microchannels". *J. Heat Transfer,* **136**(1).

[15] Ng, C., and Wang, C. Y., 2014. "Temperature jump coefficient for superhydrophobic surfaces". *J. Heat Transfer,* **136**(6).

[16] Maynes, D., Webb, B. W., and Davies, J., 2008. "Thermal transport in a microchannel exhibiting ultrahydrophobic microribs maintained at constant temperature". *J. Heat Transfer,* **130**(2), p. 022402.

[17] Maynes, D., Webb, B. W., Crockett, J., and Solovjov, V., 2013. "Analysis of laminar slip-flow thermal transport in microchannels with transverse rib and cavity structured superhydrophobic walls at constant heat flux". *J. Heat Transfer,* **135**(2), p. 021701.

[18] Patankar, S. V., Liu, C. H., and Sparrow, E. M., 1977. "Fully developed flow and heat transfer in ducts having streamwise-periodic variations of cross-sectional area". *Int. J. Heat Mass Transf.*

[19] Maynes, D., and Crockett, J., 2014. "Apparent temperature jump and thermal transport in channels with streamwise rib and cavity featured superhydrophobic walls at constant heat flux". *J. Heat Transfer,* **136**(1), p. 011701.

[20] Kirk, T. L., Hodes, M., and Papageorgiou, D. T., 2017.

"Nusselt numbers for poiseuille flow over isoflux parallel ridges accounting for meniscus curvature". *J. Fluid Mech.,* **811**, pp. 315–349.

[21] Hodes, M., Zhang, R., Lam, L. S., Wilcoxon, R., and Lower, N., 2014. "On the potential of galinstan-based minichannel and minigap cooling". *IEEE Trans. Compon. Packag. Manuf.,* **4**(1), pp. 46–56.

[22] Lam, L. S., Hodes, M., and Enright, R., 2015. "Analysis of galinstan-based microgap cooling enhancement using structured surfaces". *J. Heat Transfer,* **137**(9), p. 091003.

[23] Liu, T., Sen, P., and Kim, C., 2011. "Characterization of nontoxic liquid-metal alloy galinstan for applications in microdevices". *J. Microelectromechanical Syst.,* **21**(2), pp. 443–450.

[24] Tam, D., von ARNIM, V., McKinley, G. H., and Hosoi, A. E., 2009. "Marangoni convection in droplets on superhydrophobic surfaces". *J. Fluid Mech.,* **624**, pp. 101–123.

[25] Baier, T., Steffes, C., and Hardt, S., 2010. "Thermocapillary flow on superhydrophobic surfaces". *Phys. Rev. E,* **82**(3), p. 037301.

[26] Game, S., Hodes, M., Kirk, T., and Papageorgiou, D. T., 2018. "Nusselt numbers for poiseuille flow over isoflux parallel ridges for arbitrary meniscus curvature". *J. Heat Transfer,* **140**(8), p. 081701.

[27] Bergman, T. L., Incropera, F. P., DeWitt, D. P., and Lavine, A. S., 2011. *Fundamentals of heat and mass transfer*. John Wiley & Sons.

[28] Peyret, R., 2013. *Spectral methods for incompressible viscous flow*, Vol. 148. Springer Science & Business Media.

[29] Keyes, R. W., 1975. "Physical limits in digital electronics". *Proc. IEEE,* **63**(5), pp. 740–767.

[30] Lemmon, E. W., 1998. "Thermophysical properties of fluid systems". *NIST chemistry WebBook*.

[31] Prokhorenko, V. Y., Roshchupkin, V. V., Pokrasin, M. A., Prokhorenko, S., and Kotov, V., 2000. "Liquid gallium: potential uses as a heat-transfer agent". *High Temp.,* **38**(6), pp. 954–968.